UC Santa Barbara

UC Santa Barbara Electronic Theses and Dissertations

Title

The Bowing Parameter of Low Indium Content InGaN

Permalink

https://escholarship.org/uc/item/2ww5053h

Author

Pivard, Camille Y.

Publication Date

2023

Peer reviewed|Thesis/dissertation

UNIVERSITY OF CALIFORNIA

Santa Barbara

The Bowing Parameter of Low Indium Content InGaN

A thesis submitted in partial satisfaction of the

requirements for the degree Master of Science

in Materials Science

by

Camille Y. Pivard

Committee in charge:

Professor James S. Speck, Chair

Professor Steven P. DenBaars

Professor Sriram Krishnamoorthy

September 2023

The thesis of Camile Y. Pivard is approved.

_____

Steven P. DenBaars

_____

Sriram Krishnamoorthy

_____

James S. Speck, Committee Chair

June 2023

The Bowing Parameter of Low Indium Content InGaN

Copyright © 2023

by

Camille Y. Pivard

ACKNOWLEDGEMENTS

ABSTRACT

The Bowing Parameter of Low Indium Content InGaN

by

Camille Y. Pivard

The bandgap bowing parameter of indium gallium nitride (InGaN) semiconductor alloy is of great interest. Simulations of locally disordered InGaN material such as the ones used in an application of the Landscape theory of localization require a reliable bowing parameter value for low indium content InGaN. However, current scientific literature demonstrates a wide variation[1-9] in the value of the InGaN bowing parameter.

The current study aims to use well adapted experimental and data analysis techniques to obtain a sound result. High quality thin-film InGaN light emitting diode (LED) structures with varying indium content are grown by metal organic chemical vapor deposition (MOCVD). Their composition and the thicknesses of cap GaN and InGaN layers are determined via a Rigaku high-resolution X-ray diffractometer (HRXRD). The optical transmittance (OT) is obtained using a Shimadzu UV-Vis-NIR Spectroscopy.

To ensure the dependability of the result, the experimental procedure uses a mask to expose the same small and localized area of the sample structures for both X-ray and optical measurements. The OT measurement technique avoids the Stoke shift induced error in the bandgap determination. Such error most likely occurs in emission-based measurement techniques.

The experimental data are then analyzed using the transfer matrix method (TMM) for the InGaN absorption coefficient. The latter allows for bandgap determination using Tauc plots. The resulting low indium content ($8\% \leq x \leq 15\%$) fully strained InGaN bowing parameter is $2.55\ eV$. In the same composition range, the InGaN strain corrected bowing parameter is $3.65\ eV$.

An alternative InGaN absorption coefficient extraction method is also used for comparison. The single slab approximation method assumes that the multilayer structure can be considered as a single slab with infinite internal reflections and only the InGaN layer is effectively absorbing. This method yields the bowing parameters of $2.15 eV$ and $3.2 eV$ for fully strained and strain corrected InGaN structures respectively.

The TMM is concluded to be the superior method for absorption coefficient extraction of the InGaN multilayer heterostructure. Ideas for future work are discussed.

TABLE OF CONTENTS

LIST OF FIGURES

I. Introduction and background

The indium gallium nitride (InGaN) light-emitting diode (LED) is not only useful in solving the world's energy crisis but is also an interesting semiconductor to study in theoretical terms. Possessing many special material properties, the $In_xGa_{1-x}N$ alloy follows a deviation from the empirical Vegard's law in terms of how its bandgap energy relates to its composition. x represents the indium composition. The bowing parameter describes how much this relationship deviates from linearity.

The bowing parameter plays an important role in the design, engineering, and fabrication of InGaN based optoelectronic devices. It enables control over bandgap energy and improves device efficiency. It is also crucial in validating theoretical models and in predicting material properties.

The bowing parameter is used in the application of the Localization landscape theory of disorder in semiconductors[3] in the Simons Collaboration on Localization of Waves. It is used in modeling disordered quantum effects in the carrier transport and recombination of InGaN LEDs. The random alloy generator simulates data points with random variation in composition ($10\% \leq x \leq 30\%$) hence bandgap value. The bowing parameter of $1.4eV$ was used in Li et al.'s study[3].

The wide variation in the value of the InGaN bowing parameter and in the methods used to find it in literature present a challenge in selecting a trustworthy value. Some sources support that $b_{InGaN} = 1.4\ eV$. For example, Kudrawiec et al.[4] determined the values $1.4 \pm 0.2\ eV$ and $2.1 \pm 0.3\ eV$ with and without strain correction using contactless electroreflectance (CER) and photoluminescence (PL). Wu et al.[5] obtained $1.4\ eV$ using photo-modulated transmission (PT) and optical absorption for indium rich InGaN alloy ($x > 50\%$). Yet many more differ in

their findings. Sakalauskas et al.'s [6] ab initio and spectroscopic ellipsometry based study on GaN rich strain free InGaN yielded a bowing of $1.65 \pm 0.07 eV$. A study based on the PL through the whole composition range by Moret[7] concluded that $b = 2.8\ eV$.

Some studies include variations in the strain profile of the InGaN heterostructure. Orsal et al.[8] used cathodoluminescence (CL) and a corresponding hyperspectral map on both relaxed and strained InGaN layers to determine that they had bowings of $2.70 \pm 0.12\ eV$ and $1.32 \pm 0.28\ eV$ respectively. On the other hand, Van de Walle et al.[9] stated that ab initio calculation based on pseudopotential-density functional theory showed strong composition-dependence and that for InGaN compositions of $x = 0.0625, 0.125, 0.25$ the bowing parameter varied respectively as $4.8, 3.5, 3.0\ eV$. They also experimentally employed optical transmission (OT) spectroscopy and Rutherford backscattering spectrometry (RBS) to find a bowing value of $3.8\ eV$ at $x = 0.1$ for pseudomorphically strained samples. They claimed that for relaxed layers the estimate should be lower, but still greater than $3.0 eV$.

The discrepancy in reported bowing parameter values from simulation and experiments originate from many factors. The present study seeks to experimentally determine the InGaN bowing parameter at low indium composition where $8\% < x < 15\%$.

Moses et al.[10] demonstrated that the bowing parameter depends on the indium composition through simulation: at low indium composition, the bowing is expected to be higher. Kazazis et al.[11] provided insight into experimental techniques have varying degrees of effectiveness: the widely used emission techniques such as PL and CL are less adequate than OT or optical absorption (OA) measurements. The challenge of underestimating the bandgap energy using emission techniques originates from the Stoke shift that comes from the InGaN alloy's compositional inhomogeneities[12,13] and further inherent random alloy hole localization[14,15].

The paper mentions two shortcomings of this better method however: the energy dependence of the refractive index is not accounted for; strain and relaxation effects would change the bowing parameter. The epitaxial strain induced biaxial compressive stress and layer thickness variation[16] in the sample structure would produce a blueshift in the bandgap.
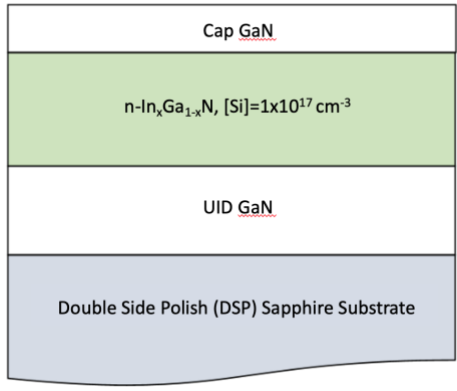
Figure 1. Diagram (Courtesy of C. Lynsky) showing the structure of the InGaN samples used in this study. x is the percentage of indium content.

In this study, the more appropriate optical transmittance measurement technique is used. The high quality thin-film samples are epitaxially grown on metalorganic chemical vapor deposition (MOCVD) in the UCSB Materials Department MOCVD Laboratory by Dr. Cheyenne Lynsky. Their structure is shown in Fig.1. The GaN capped InGaN layer is grown on an unintentionally doped thick GaN layer on a DSP sapphire substrate. X-Ray diffraction rocking curve measurements and analyses are used for InGaN composition, cap GaN and InGaN layer thickness estimates. Reciprocal space mapping (RSM) analysis is used to confirm that the InGaN layers are fully strained on the GaN layers and to obtain strain information. Two techniques are used to obtain the InGaN bowing parameter at low indium composition range ($8\% < x < 15\%$). In the transfer matrix method (TMM), the multilayer structure's

layer thicknesses and energy dependent complex refractive indices including the InGaN energy dependent refractive index are accounted for in the analysis of the InGaN absorption coefficient extraction from experimental results. The bandgap energies are extracted using Tauc plots and fitted to the InGaN bandgap energy equation, a modified Vegard's law to obtain the bowing parameter. The resulting bowing parameters for fully stained and strain corrected InGaN at low indium compositions ($8\% < x < 15\%$) are respectively $2.55eV$ and $3.65\ eV$. These values align with the findings or Orsal et al.[8] and Van der Walle et al.[9].

In the single slab approximation method, the multilayer structure is considered as a single slab with infinite internal reflections. The InGaN layer is the seen as the only effectively absorbing layer. The Tauc plot bandgap extraction method and the strain adjustment are still applied in this analysis. The bowing parameters obtained are $2.15eV$ for fully strained InGaN structures and $3.2eV$ for the strain corrected InGaN structures. These values are significantly lower than the TMM findings. The TMM is concluded to be the superior method for extracting the InGaN absorption coefficient for reasons stated in the "results and discussion" section.

II. Experimental methods

A. Measurement methods

1. Optical absorption measurements

The optical transmittance and reflectance of each sample are measured by the Shimadzu UV 3600 UV-Vis-NIR Spectrometer which uses a $BaSO_4$ coated integrating sphere. Fig. 2 shows schematic diagrams of the inside of the integrating sphere. The transmittance of a sample is measured relative to a reference as shown on the left of Fig. 2. The reference measurement achieving 100% transmittance is done with air instead of the sample. The reflectance measurement is illustrated on the right of Fig.2. The light bouncing off the sample is measured relative to the same measurement done with a $BaSO_4$ white plate as the 100% reflectance reference. On Fig. 2, R is the reference light beam and S is the sample beam. Both are measured in the 300 nm-600 nm range using a photodiode detector which is installed on the top of the integrating sphere. The spectral resolution is within $20\ nm$.
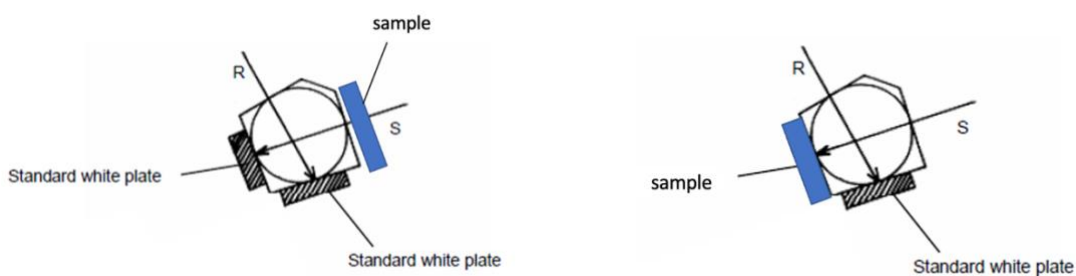
Figure 2. Diagrams of inside of the integrating sphere for transmittance measurement (left) and reflection measurement (right) adapted from the instrument's User Guide[1].

R is the reference light beam and S is the sample beam. The photodiode detector (not shown) is installed on top of the sphere.

Due to the non-uniformity of layer thickness on the sample wafer, the ability to localize a small area at the center of the sample is desired. A custom-made mask (Fig.3) with a $9\ mm \times 6\ mm$ aperture and a sample holder was designed and fabricated by the machine shop for highly reproducible results. The mask is coated in black anodized aluminum so that it does not contribute to the optical measurements. The mask's aperture was optimized through experimental trial and error. It is small enough to localize an area with uniform layer thickness, while also capturing enough light, around 60% of light source intensity, to achieve stable signal intensity.
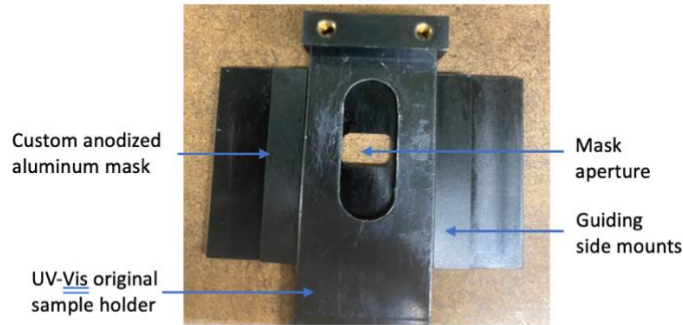
Figure 3. Labeled diagram of custom-made anodized aluminum optical measurement mask.

2. High-Resolution X-Ray Diffraction (HRXRD) measurements

The indium content and InGaN and GaN layer thicknesses are obtained by analyzing X-Ray Diffraction (XRD) data. The XRD measurements are triple-axis omega-two theta scans done

on the (002) reflection using a Rigaku HyPix 2000 XRD machine with a Ge (220) crystal monochromator. The sample is centered on the stage to expose target area which corresponds to the mask aperture of the optical measurement. It is exposed to a $12\ mm \times 2.3\ mm$ X-Ray beam. (Fig. 4)
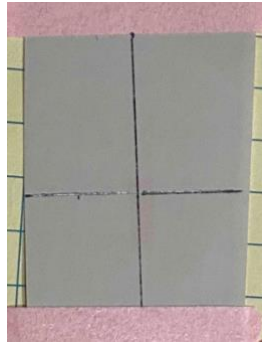
Figure 4. Faint trace of beam on X-Ray burn paper showing an area of 12mm by 2.3mm.

B. Data analysis methods

1. Estimation of thick GaN thickness using Fabry-Perot fringes

Far away from the absorption edge, the Fabry-Perot fringes on the wavelength dependent transmittance intensity can in theory be used to estimate the thickness of the thick UID GaN layer. The Fabry-Perot cavity thickness l is related to the nearest neighbor crest to crest wavelength difference between adjacent fringes $\Delta\lambda$, the refractive index n_g, the reference wavelength λ_0, the incident beam angle θ by the following equation[17]:

$$l \approx \frac{\lambda_0^2}{2\, n_g\, \Delta\lambda\, Cos(\theta)}$$

1

2. Rigaku HRXRD plug-in peak fitting

The thicknesses of the cap GaN layer and of the InGaN layer as well as the indium content of the sample can be obtained by analyzing the Rigaku High-Resolution XRD rocking-curve data in the Rigaku HRXRD plug-in simulation and fitting software[18].

Given the sample structure, the program would fit the Bragg peaks and satellite peaks on the rocking curve. First, it uses generic algorithm to perform a global search for the solution and grossly locates the neighborhood of the optimal solution. Then, the Quasi-Newton least squares method or the Nelder-Mead method is used to refine the solution. Elastic strain information is also considered. Additionally, the incident X-ray divergence is convoluted with the theoretical rocking-curve as the pseudo-Voigt function.

This method is more accurate than estimating the InGaN layer thickness only using Bragg's law [19]:

$$\lambda = 2d_{hkl} \sin \theta_B$$

Eq. 2

where λ is the x-ray wavelength ($\lambda_{CuK\alpha_1} = 1.5405974$ Å), d is the spacing of the diffracting planes from the (hkl) reflection, and θ_B is the Bragg angle.

Dr. Kelsey Jorgensen wrote a MATLAB Indium composition extraction code that follows these steps: Using the (002) reflection, $d_{002}^{GaN} = \frac{1}{2} c_{GaN}$ where $c_{GaN} = 5.1855$Å is the reference GaN lattice parameter[20]. The GaN Bragg angle is $\theta_{002}^{GaN} = \sin^{-1} \frac{\lambda}{2d_{002}^{GaN}}$. The measured GaN-

InGaN peak separation is $\Delta\theta = \theta_{002}^{InGaN} - \theta_{002}^{GaN}$ and the measured $d_{002}^{InGaN} = \frac{\lambda}{2\sin(\theta_{002}^{GaN}+\Delta\theta)}$.

Assuming that the InGaN layer is fully strained, its composition can be obtained as

$c_{meas}^{InGaN} = 2d_{002}^{InGaN}$.

3. Layer strain from Reciprocal Space Mapping (RSM)

The lattice mismatch and the pseudomorphic strain present between the UID GaN layer and the epitaxial InGaN layer can be measured by analyzing the reciprocal space map (RSM). The in-plane and out-of-plane peak positions of GaN $Q_{x,GaN}$, $Q_{z,GaN}$ and of InGaN $Q_{x,InGaN}$, $Q_{z,InGaN}$ are used to compute the sample InGaN lattice parameters:

$$a_{InGaN} = \frac{Q_{x,GaN}}{Q_{x,InGaN}} \times a_{GaN} \qquad \textbf{Eq. 3}$$

$$c_{InGaN} = \frac{Q_{x,GaN}}{Q_{x,InGaN}} \times c_{GaN} \qquad \textbf{Eq. 4}$$

The raw data (cf. angle maps in Appendix C) is processed in Dr. Chris Zollner's MATLAB peak finding code to produce values in unit of position instead of angles. The GaN lattice parameters[20] are $a_{GaN} = 3.1896$Å and $c_{GaN} = 5.1855$Å and the InN lattice parameters[21] are $a_{InN} = 3.5378$Å and $c_{InN} = 5.7033$Å.

The fully relaxed InGaN lattice parameters $a_{InGaN}^{fully\ relaxed}$ and $c_{InGaN}^{fully\ relaxed}$ with known indium composition x can be obtained via the Vegard's law:

$$a_{InGaN}^{fully\ relaxed} = x\ a_{InN} + (1-x)\ a_{GaN} \qquad \textbf{Eq. 5}$$

$$c_{InGaN}^{fully\ relaxed} = x\ c_{InN} + (1-x)\ c_{GaN} \qquad \textbf{Eq. 6}$$

9

Since the in-plane direction is within the surface plane, perpendicular to the growth direction, the degree of relaxation of the layer is:

$$\% \ relaxation = \frac{a_{InGaN} - a_{GaN}}{a_{InGaN}^{fully\ relaxed} - a_{GaN}} \times 100 \qquad \textbf{Eq. 7}$$

The InGaN layer's in-plane strain[22] is defined as:

$$\epsilon_{||} = \epsilon_{||}^{InGaN} = \frac{a_{InGaN} - a_{InGaN}^{fully\ relaxed}}{a_{InGaN}^{fully\ relaxed}} \qquad \textbf{Eq. 8}$$

4. Extraction of the absorption coefficient via the single slab infinite internal reflection summation

Let a single slab of material of thickness X have reflectivity $\bar{R}$, reflectance R, absorption coefficient α, and transmittance T. Here, the term reflectivity refers to how much light is reflected off a surface upon the light's first contact with a surface whereas reflectance is the total light bouncing back from both interfaces of a slab of material. Transmittivity and transmittance are defined similarly for light passing through an interface of a slab of material. Assume that the incident ray intensity I_0 is unity, i.e., $I_0 = 1$. Each time a ray of light crosses the boundary of the sample, its intensity picks up a $1 - \bar{R}$ term. Each time it is reflected at the boundary of the sample, it picks up a term $\bar{R}$. Each time a ray of light travels across the sample it picks up a decay term $e^{-\alpha l}$ according to the Beer-Lambert law[23]. Fig. 5 illustrates the trajectory of the light ray through the medium with multiple internal reflections.

10
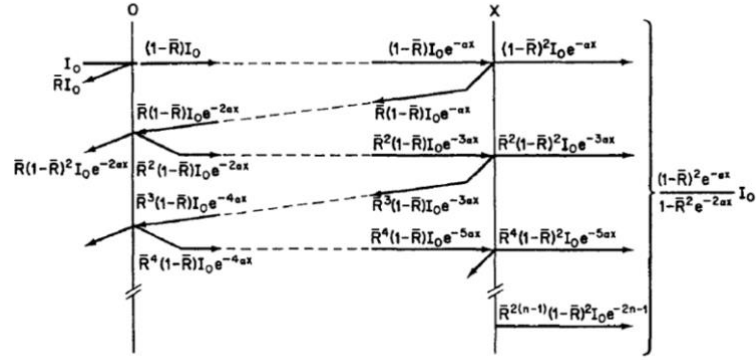
Figure 5. Schematic diagram of energy flow in a material with internal reflections adapted from Pankove[2], Chapter 4. The light ray trajectory as a series of transmissions and reflections across a single slab of material is shown. The normally incident ray has intensity I_0. The material has thickness X, absorption coefficient α, total transmittance T and simple reflectance $\bar{R}$.

The total transmittance through the single slab is the sum $T = \Sigma_i \tau_i$ where τ_i is the coefficient of the light intensity of ith transmission. The first term in the sum is $\tau_1 = (1 - \bar{R})^2 e^{-\alpha X}$. The second transmission term τ_2 is the result of two internal reflections $\bar{R}^2$, the decay over length $3X$ as the exponential term $e^{-3\alpha X}$, and the transmission across the sample boundaries $(1 - \bar{R})^2$. Therefore, $\tau_2 = \bar{R}^2 (1 - \bar{R})^2 e^{-3\alpha X} = \tau_1 r$ where $r = \bar{R}^2 e^{-2\alpha X}$. Each subsequent transmission term would pick up an additional factor of r.

Expanding the sum and using the geometric series formula,

$$T = \lim_{n \to \infty} \Sigma_0^n \tau_1 r^i = \lim_{n \to \infty} \tau_1 \Sigma_0^n r^i = \lim_{n \to \infty} \tau_1 \frac{1 - r^{n+1}}{1 - r} \qquad \textbf{Eq. 9}$$

11

Since $-1 < r < 1$,

$$T = \frac{(1-\bar{R})^2 e^{-\alpha X}}{1 - \bar{R}^2 e^{-\alpha X}}$$
Eq. 10

The absorption coefficient[2] of a single slab sample of known length X will be given by rearranging Eq. 10:

$$\alpha = \frac{1}{-X} \ln \left[\frac{-(1-\bar{R})^2 \pm \sqrt{(1-\bar{R})^4 + 4T^2\bar{R}^2}}{2T\bar{R}^2} \right]$$
Eq. 11

where $\bar{R} = \frac{R}{2-R}$.

This method of obtaining the absorption coefficient is effective when the material of interest is a single slab. In the case of the multilayer InGaN structure in this study, it can be assumed that far below the GaN bandgap energy ($< 3.3 eV$), the InGaN bandgap energy is below that of GaN, the GaN absorption coefficient is negligeable below the GaN bandgap energy, and that the sapphire substrate is not at all absorptive. Under these assumptions, the stack of materials can be considered as effectively a single slab of InGaN.

In the energy region far below the InGaN bandgap energy where the InGaN absorption is negligible ($\alpha \approx 0$), the absorptance A or the fraction of the incident light that's absorbed by the sample is zero. Since $A + T + R = 1$[24], it can be assumed that $R = 1 - T$. In terms of $\bar{R}$, $R = \frac{2\bar{R}}{1+\bar{R}}$. In this region, the transmittance can be linearly fitted and used to yield the reflectance. The reflectance over the entire energy range can be extrapolated by extending the

linear fit. The linear fit extrapolation has the advantage of being a good approximation and of avoiding the usage of experimental reflectance data which is too noisy for analysis.

5. Extraction of the absorption coefficient via the Transfer Matrix Method (TMM)

The structure of interest is a multilayer heterostructure, therefore the TMM is appropriate. The TMM combines the optical transmittance and reflectance information of multiple layers and produces the equivalent information of a stacked multilayer. The information in this section is based on Peumans et al.[25], Pettersson et al.[26] and Katsidis et al.[27].

The TMM varies in treating optical transmittance and reflectance of systems with different types of coherence. The origins of the different coherences are explained in detail in Katsidis et al.'s work[27]. For simplicity, coherent layers are thin, homogeneous, optically isotropic, and have planar and parallel interfaces. Incoherence arises from thick films or ones with nonparallel surfaces.

The coherence length[28] indicates how a layer's thickness correlates to the coherence. If a material layer is thicker than the coherence length, it is considered a thick film with incoherence. The coherence length for the InGaN multilayer stack is on the order of $\frac{\lambda^2}{n\Delta\lambda}$ where λ is the source central wavelength, n is the refractive index of the layer and $\Delta\lambda$ is the source spectral width. The parameters λ, n, and $\Delta\lambda$ are on the orders of $10^{-7}m$, 0 and $10^{-8}m$ respectively. Thus, the InGaN multilayer structure's coherence length should be on the order of $10^{-6}m$.

Partial coherence is a third case which is usually due to surface or interface roughness. The reflected and transmitted beams are phase shifted with respect to each other. The irregularities can be modeled as a Gaussian distribution. The TMM for this case will not be considered here.

a. Coherent interference

Consider the case of thin layers of material which allows for coherent interference or the addition of waves of the same frequency and waveform. The thickness of the material is within the coherence length, within which propagating waves maintain their level of coherence[30].

i. Propagation across a boundary
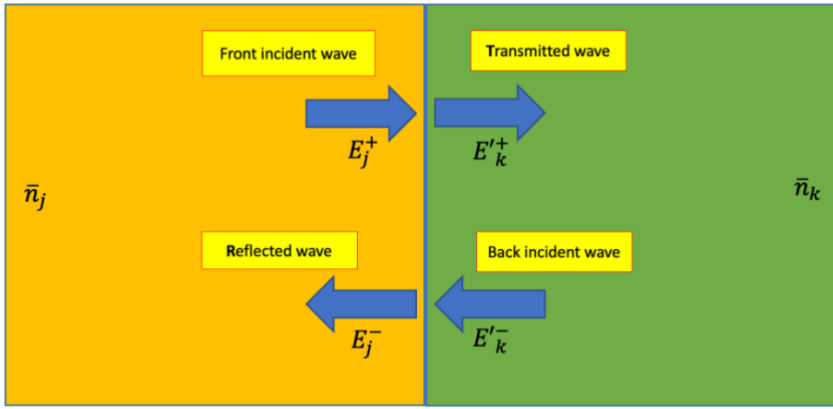
Figure 6. Schematic diagram of the light ray trajectory as it crosses the boundary between two media at normal incidence in terms of transfer matrix collective waves. The media has refractive indices $n1$ and $n2$.

The complex refractive index[29] of the jth layer of medium is $\bar{n}_j = n_j + i\kappa_j$ where n_j is the refractive index and κ_j is the extinction coefficient. In the Beer-Lambert law, the intensity of the electromagnetic wave or light with wavelength λ propagating in the x direction is expressed as $I(x) = I_0 e^{-\frac{4\pi\kappa x}{\lambda}}$. The absorption coefficient[30] α is defined such that $I(x) = I_0 e^{-\alpha x}$. Therefore,

14

$$\alpha = \frac{4\pi\kappa}{\lambda} \qquad\qquad \textbf{Eq. 12}$$

Due to this relation, "extinction coefficient" and "absorption coefficient" are used interchangeable in the remainder of the text.

When a light ray crosses, at normal incidence, from the jth layer to the kth layer of media (Fig. 6) with respective refractive indices $\bar{n}_j$ and $\bar{n}_k$, the transmission coefficient $t_{j,k}$ and reflection coefficient $r_{j,k}$ can be directly obtained by using Fresnel's equations:

$$t_{j,k} = \frac{2\bar{n}_j}{\bar{n}_j + \bar{n}_k} \qquad\qquad \textbf{Eq. 13}$$

and

$$r_{j,k} = \frac{\bar{n}_j - \bar{n}_k}{\bar{n}_j + \bar{n}_k} \qquad\qquad \textbf{Eq. 14}$$

The forward and backward traveling optical electric fields $\bar{E}_j^+$ and $\bar{E}_j^-$ in layer j are related to the corresponding $\bar{E'}_k^+$ and $\bar{E'}_k^-$ in layer k via the interface matrix $I_{j,k}$. The $'$ on the electric field denotes that it occurs right after an interface in the forward traveling direction. Its absence denotes that the electric field is found right before an interface in the forward traveling direction. The relation is therefore:

$$\begin{pmatrix} \bar{E}_j^+ \\ \bar{E}_j^- \end{pmatrix} = I_{j,k} \begin{pmatrix} \bar{E'}_k^+ \\ \bar{E'}_k^- \end{pmatrix} \qquad\qquad \textbf{Eq. 15}$$

where

$$I_{j,k} = \frac{1}{t_{j,k}} \begin{bmatrix} 1 & r_{j,k} \\ r_{j,k} & 1 \end{bmatrix} \qquad\qquad \textbf{Eq. 16}$$

15

Propagation through a homogeneous medium
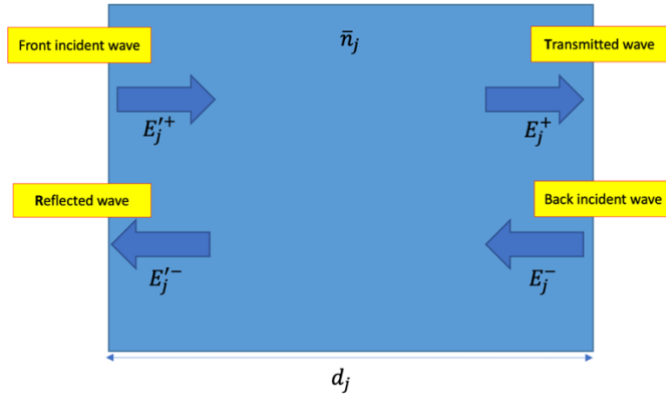
Figure 7. Schematic diagram of the optical electric field trajectory as it enters a single layer j of homogeneous medium that both transmits and reflects at normal incidence in terms of transfer matrix collective waves. The propagation medium has refractive index $\bar{n}_j$ and thickness d_j.

When light propagates through a single slab of homogeneous medium (Fig. 7) in layer j that has complex refractive index $\bar{n}_j$ and thickness d_j, the traveling wave of wavelength λ picks up both a propagation phase factor $e^{-i\phi_j d_j}$ where $\phi_j = \frac{2\pi n_j}{\lambda}$ is dimensionless and an attenuation factor $e^{-\alpha_j d_j}$ due to optical absorption where $\alpha_j = \frac{4\pi \kappa_j}{\lambda}$.

In the forward traveling direction, the forward and backward traveling optical electric fields have complex wave amplitudes $\bar{E}'^{+}_j$ and $\bar{E}'^{-}_j$ at the beginning of layer j are related to the corresponding complex wave amplitudes $\bar{E}^{+}_j$ and $\bar{E}^{-}_j$ at the end of layer j via the layer matrix L_j s.t.

$$\begin{pmatrix} \bar{E}'^{+}_{j} \\ \bar{E}'^{-}_{j} \end{pmatrix} = L_j \begin{pmatrix} \bar{E}^{+}_{j} \\ \bar{E}^{-}_{j} \end{pmatrix}$$

<div align="right">**Eq. 17**</div>

The layer matrix is a 2×2 matrix,

$$L_j = \begin{bmatrix} e^{-i\xi_j d_j} & 0 \\ 0 & e^{i\xi_j d_j} \end{bmatrix}$$

<div align="right">**Eq. 18**</div>

where $\xi_j = \left(\frac{2\pi}{\lambda}\right)\bar{n}_j$ and $\bar{n}_j = n_j + \kappa_j$.

    iii.   General transfer matrix for coherent interference
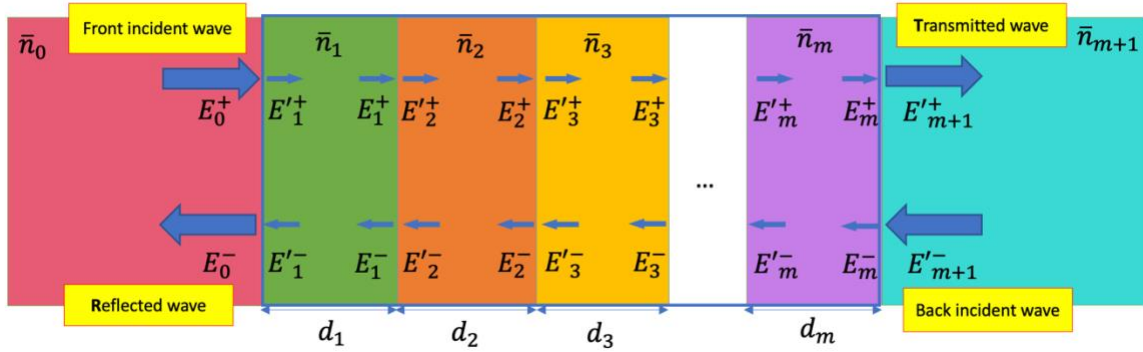
Figure 8. Schematic diagram of the wave trajectory as it enters a stack of m coherent layers of materials that both transmits and reflects at normal incidence. Each layer of material has its corresponding complex refractive index $\bar{n}$ and thickness d. The media on both ends of the stack are semi-infinite. The waves outside of the stack of materials are the collective transfer matrix waves.

Suppose a light wave enters a stack m layers of materials (Fig. 8). The initial semi-infinite medium of the material is indexed layer 0. The final semi-infinite medium of the material is indexed layer $m + 1$. In the forward traveling direction, the forward and backward traveling optical electric fields $\bar{E}^{+}_{0}$ and $\bar{E}^{-}_{0}$ immediately preceding the first material boundary in layer 0

are related to the corresponding $\bar{E}'^{+}_{m+1}$ and $\bar{E}'^{-}_{m+1}$ immediately following the last material boundary in layer $m + 1$ via the transfer matrix M of the whole stack of finite materials as follows:

$$\begin{bmatrix} \bar{E}^{+}_0 \\ \bar{E}^{-}_0 \end{bmatrix} = M \begin{bmatrix} \bar{E}'^{+}_{m+1} \\ \bar{E}'^{-}_{m+1} \end{bmatrix} \qquad \textbf{Eq. 19}$$

The transfer matrix M captures all optical transmission, reflection, and absorption activities throughout the stack of material separating the two semi-infinite media in a single 2×2 matrix.

$$M = \begin{bmatrix} M_{11} & M_{12} \\ M_{21} & M_{22} \end{bmatrix} = \left(\prod_{n=1}^{m} I_{n-1,n} L_n \right) \cdot I_{m,m+1} \qquad \textbf{Eq. 20}$$

Each layer n of the stack has two interfaces $(n - 1, n)$ and $(n, n + 1)$ and a finite thickness d_n. Each interface crossing is represented by an interface matrix I and each layer propagation is represented by a layer matrix L. The M matrix is the production of all the $m + 1$ interface matrices and m layer matrices in the order of forward wave propagation.

Adding precision to the notation, the initial and final layers i and f of the stack can be indicated by indexing the transfer matrix M as $M_{i/f}$. Each of its components can be expressed in terms of the complex Fresnel's transmission coefficient $t_{p,q}$ and reflection coefficient $r_{p,q}$ at normal incidence where the indices p and q are either 0 and $m + 1$ or vice versa depending on the direction of the wave propagation in question:

$$M = M_{0/(m+1)} = \begin{bmatrix} M_{11} & M_{12} \\ M_{21} & M_{22} \end{bmatrix} \qquad \textbf{Eq. 21}$$

$$= \frac{1}{t_{0,m+1}} \begin{bmatrix} 1 & -r_{m+1,0} \\ r_{0,m+1} & t_{0,m+1}t_{m+1,0} - r_{0,m+1}r_{m+1,0} \end{bmatrix}$$

18

The front transmission and reflection coefficients t and r and back transmission and reflection coefficients t' and r' can in turn be expressed in terms of the M matrix elements or in terms of quotients of complex wave amplitudes as follows:

$$t = t_{0,m+1} = \frac{\bar{E}_{m+1}^+}{\bar{E}_0^+} = \frac{1}{M_{11}} \qquad \textbf{Eq. 22}$$

$$r = r_{0,m+1} = \frac{\bar{E}_0^-}{\bar{E}_0^+} = \frac{M_{21}}{M_{11}} \qquad \textbf{Eq. 23}$$

$$t' = t_{m+1,0} = \frac{\bar{E}_0^-}{\bar{E}_{m+1}^+} = \frac{Det\ M}{M_{11}} \qquad \textbf{Eq. 24}$$

$$r' = r_{m+1,0} = \frac{\bar{E}_{m+1}^-}{\bar{E}_{m-1}^+} = -\frac{M_{12}}{M_{11}} \qquad \textbf{Eq. 25}$$

where $Det\ M = M_{11}M_{22} - M_{12}M_{21}$.

The front transmittance and reflectance T and R and back transmittance and reflectance T' and R' in the direction of forward wave propagation are the square of the magnitude of the corresponding complex reflection and transmission coefficients:

$$T = |t|^2 \qquad \textbf{Eq. 26}$$

$$R = |r|^2 \qquad \textbf{Eq. 27}$$

$$T' = |t'|^2 \qquad \textbf{Eq. 28}$$

$$R' = |r'|^2 \qquad \textbf{Eq. 29}$$

b. Transfer matrix under fully incoherent interference
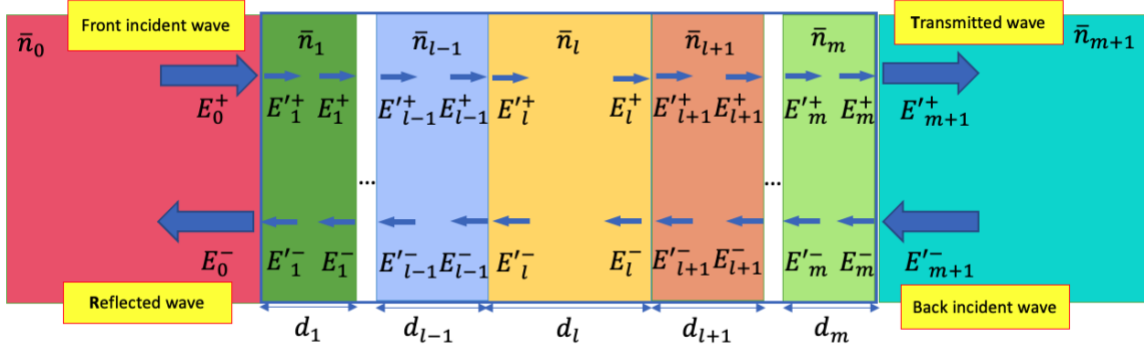
Figure 9. Schematic diagram of the wave trajectory as it enters a stack of m layers of materials that both transmits and reflects at normal incidence. All layers except layer l are coherent. Each layer of material has its corresponding complex refractive index $\bar{n}$ and thickness d. The media on both ends of the stack are semi-infinite. The waves outside of the stack of materials are the collective transfer matrix waves.

When a material layer, say layer l, largely exceeds the coherence length, then it becomes the case of fully incoherent interference. To treat this case as illustrated in Fig. 9, the general transfer matrix $M_{0/m+1}^{incoherent}$ will be comprised of the incoherent layer matrix $L_l^{incoherent}$ for wave propagation through the incoherent layer and of the two transfer matrices $M_{0/l}^{incoherent}$ and describing the wave through the stacks preceding and following the incoherent layer $M_{l/m+1}^{incoherent}$.

$$M_{0/m+1}^{incoherent} = \begin{bmatrix} M_{11}^{incoherent} & M_{12}^{incoherent} \\ M_{21}^{incoherent} & M_{22}^{incoherent} \end{bmatrix} \qquad \textbf{Eq. 30}$$

$$= M_{0/l}^{incoherent} L_l^{incoherent} M_{l/m+1}^{incoherent}$$

The three component matrices are constructed following the same strategy as for the coherent case using Eq. 16, Eq. 18 and Eq. 20, but the elements of the matrices in Eq. 21 are replaced with the square of its magnitude or the sum of the square of its components in the following ways:

Eq. 31

$$M_{0/l}^{incoherent} = \frac{1}{|t_{0,l}|^2} \begin{bmatrix} 1 & -|r_{l,0}|^2 \\ |r_{0,l}|^2 & |t_{0,l}t_{l,0}|^2 - |r_{0,l}r_{l,0}|^2 \end{bmatrix}$$

$$L_l^{incoherent} = \begin{bmatrix} |e^{-i\xi_l d_l}|^2 & 0 \\ 0 & |e^{i\xi_l d_l}|^2 \end{bmatrix}$$

Eq. 32

Eq. 33

$$M_{l/m+1}^{incoherent} = \frac{1}{|t_{l,m+1}|^2} \begin{bmatrix} 1 & -|r_{m+1,l}|^2 \\ |r_{l,m+1}|^2 & |t_{l,m+1}t_{m+1,l}|^2 - |r_{l,m+1}r_{m+1,l}|^2 \end{bmatrix}$$

The transmittance and reflectance of the whole stack including the incoherent layer are directly quotients of elements of $M_{0/m+1}^{incoherent}$:

$$T_{incoherent} = \frac{1}{M_{11}^{incoherent}}$$

Eq. 34

$$R_{incoherent} = \frac{M_{21}^{incoherent}}{M_{11}^{incoherent}}$$

Eq. 35

6. Tauc plot

The bandgap value can be extrapolated empirically using the Tauc plot[31]. The quantity

$(\alpha h v)^{\frac{1}{m}}$ is plotted against energy hv where α is the absorption coefficient, h Planck's constant,

v the photon frequency. The Tauc plot follows the relation

$$\alpha h v = B(h v - E_g)^m$$

Eq. 36

where B is the band tailing parameter and E_g the bandgap energy. The value of m depends on

the type of bandgap. In the case of InGaN, a direct allowed transition occurs and therefore

$m = \frac{1}{2}$. The linear part of the Tauc plot is extrapolated to the abscissa to yield the optical

bandgap energy of InGaN.

7. InGaN bandgap energy and the Vegard's law

The Vegard's law[32] is an empirical finding which applies to the bandgap energy of a binary

semiconductor if its lattice parameter can be approximated by a linear interpolation of those

of its constituents. In such case, the binary semiconductor's bandgap energy would itself be a

linear interpolation of the bandgap energies of its constituents based on its composition. In

some cases, a deviation from linearity to achieve greater accuracy requires the addition of the

bowing parameter b, a correction factor to the Vegard's law that produces a curvature in the

bandgap energies as a function of composition. Such is the case for $In_x Ga_{1-x}N$ where x is

the composition. The InGaN bandgap energy follows the modified Vegard's law equation:

Eq. 37

$$E_{g,InGaN} = x E_{g,InN} + (1 - x) E_{g,GaN} - b x (1 - x)$$

This expression would just be the Vegard's law for InGaN, if $b = 0$.

The bandgap energies of InN and GaN are respectively 0.7 eV[33–35] and 3.4 eV[36]. The bowing parameter is fitted to Eq. 37 using the literature values of InN and GaN bandgap energies and the InGaN bandgap energies for varying indium content obtained from Tauc plots.

8. The effect of strain on bandgap

The strain shifts the InGaN bandgap energy up. For small values of x, the InGaN bandgap energy change can be approximated by the same relation for GaN's change in the lowest exitonic transition energy[9,37] (eV) as a function of compressive in-plane strain (dimensionless):

$$\Delta E_g = (-9.3\ eV)\epsilon_{||}$$

<div align="right">Eq. 38</div>

III. Results and discussion

A. On the thickness and effect of the GaN layers

1. Estimation of thick GaN layer thickness from Fabry-Pérot fringes
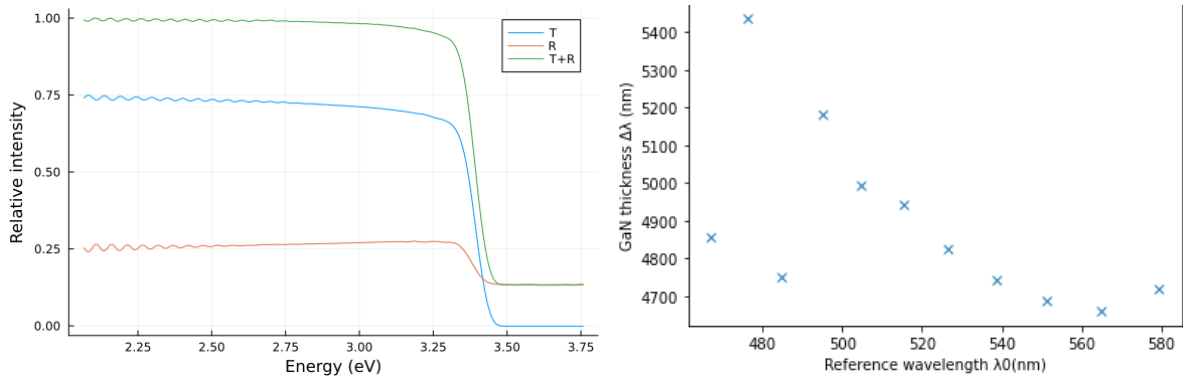
Figure 10. Left: Measured GaN on DSP sapphire optical transmittance and reflectance spectra. Right: Plot of GaN layer thickness estimate using Fabry-Pérot fringes in the transmittance data from the left plot.

The result of using Fabry-Pérot fringes for the thickness estimation (Eq.2) on a GaN on DSP sample varies with wavelength did not provide a consistent thickness as shown on Fig.10. The method provides an approximation to the material's thickness, but it is not accurate enough. The fact that transmittance and reflectance do not add up to unity in regions far below the bandgap energy on the left plot of Fig.10 shows that there is potentially partially coherent interference.

24

2. UID GaN coherence in computed optical spectra

Figure 11. Plots of the computed transmittance, reflectance, and their sum of an InGaN sample structure. The InGaN extinction coefficient is assumed to be zero. The GaN and DSP sapphire complex refractive indices are from liter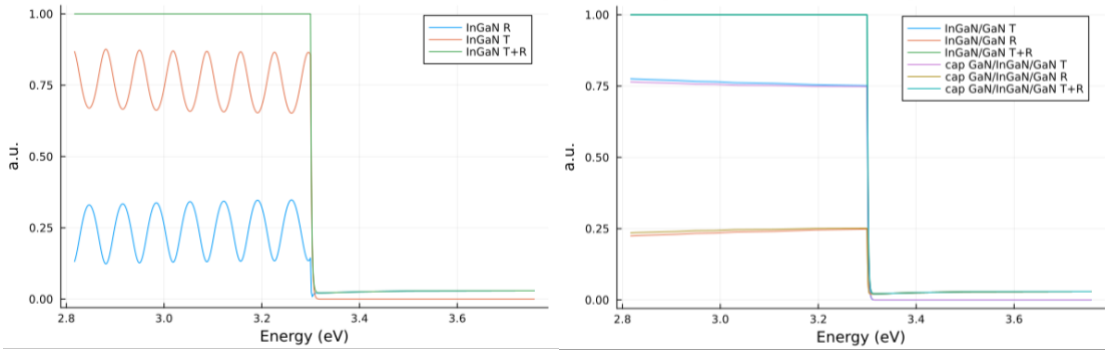ature [38,39]. The sapphire layer is assumed to be semi-infinite. Left: Cap GaN/InGaN/GaN with all layers assumed to be coherent. Right: InGaN/GaN with and without cap GaN layer with the UID GaN layer assumed to be incoherent and the other layers coherent.

The transmittance and reflectance of a complete InGaN sample structure are computed via the TMM. The important thickness of the DSP sapphire substrate allows the assumption that it is effectively a semi-infinite medium. The material layers are in the order of forward wave propagation: Al_2O_3, UID GaN, InGaN, cap GaN and air. On the left plot of Fig. 11, all layers are assumed to be coherent and their thicknesses match those present in the 11.5% indium content InGaN sample. The InGaN extinction coefficient is assumed to be zero and its refractive index is from the UCSB SSLEEC Material database[40]. The GaN and DSP sapphire extinction coefficients and refractive indices are from literature [38,39]. Accordingly, the absorption edge for GaN is 3.3 eV and its absorption coefficient below the bandgap is 0. The Fabry-Pérot fringes have very pronounced amplitudes at energies lower than that of the

absorption edge. Above the bandgap energy, most of the light is absorbed so the sum of the transmittance and reflectance remains close to zero.

The right plot of Fig.11 shows TMM calculated optical transmittance and reflectance spectra and their sum for the same InGaN structure as above with and without the cap GaN layer. In this case, the UID GaN layer is treated as an incoherent transfer matrix layer. The Fabry-Pérot fringes seen on the left plot of Fig.10 have completely disappeared. The cap GaN layer contributes to slightly lower transmittance and higher reflectance levels of the overall structure due to the GaN refractive indices in the absence of absorption below bandgap energy.

In comparison with the measured data of the same InGaN sample structure (Fig.12), the right plot in Fig.11 of the computed spectra proves to be a better correspondence than the left plot in Fig. 11. The main features that are different in the measured spectra include the small amplitude Fabry-Pérot fringes due to the UID GaN layer, the non-zero InGaN absorption and the less steep and abrupt GaN absorption edge. The lower level of transmittance and higher level of reflectance in the measured data are due to the absence of the InGaN absorption coefficient. The extinction coefficient of GaN used in the computations would also influence the resulting spectra.
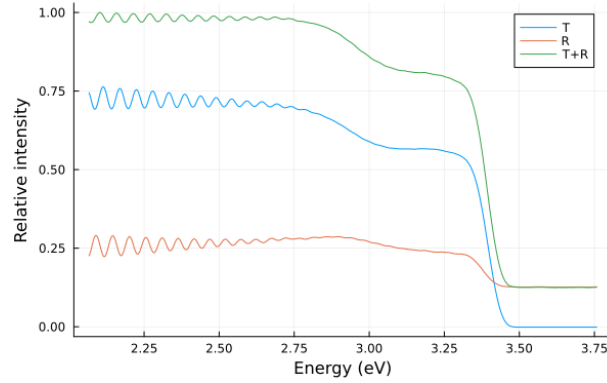
Figure 12. Plots of measured 11.5% In InGaN optical transmittance and reflectance spectra and their sum. Fabry-Pérot fringes due to the UID GaN layer are visible in all three curves at energies below $2.75eV$.

From these observations, it can be concluded that the UID GaN layer should be treated as a thick layer using incoherent TMM. This is consistent with the remark on coherence length in section II-B-5. The UID GaN thickness is on the order of μm which is on the same order as the coherence length $(10^{-6}m)$ of the InGaN multilayer structure. From this comparison, the UID GaN should be treated as an incoherent layer.

3. GaN absorption coefficient

Figure 13. Plot of the TMM extracted GaN absorption coefficient (cm^{-1}) as a function of energy (eV).

27

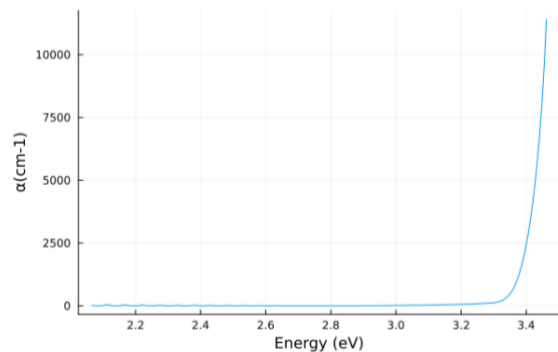The GaN absorption coefficient is extrapolated using the TMM from the measured optical transmittance data of a GaN on DSP sapphire sample and shown on Fig.13. The GaN layer is treated as incoherent, and the substrate is treated as a semi-infinite medium. The measured values are equated to the TMM calculated expression that has the GaN extinction coefficient as the sole unknown variable. The nonlinear equation is solved in Julia programming language using the function "nlsolve", a non-linear solver. Due to the multitudes of data points, the absorption edge from the results is smoother than that from Adachi[41]. The small but nonzero values in the $2.1eV$ to $2.4eV$ range, far below the bandgap energy, have considerable impact on the InGaN absorption coefficient since the UID GaN layer has an important thickness.

In fact, using GaN extinction coefficients from Adachi[41], the resulting InGaN extinction coefficients in the lower energy range became negative. It was therefore necessary to obtain more accurate GaN extinction coefficients directly using measured data. The phase shift in the transmittance and reflectance measurements of the GaN on DSP sample in the left plot of Fig.10 suggests that there might be partial coherence due to surface or interface roughness.

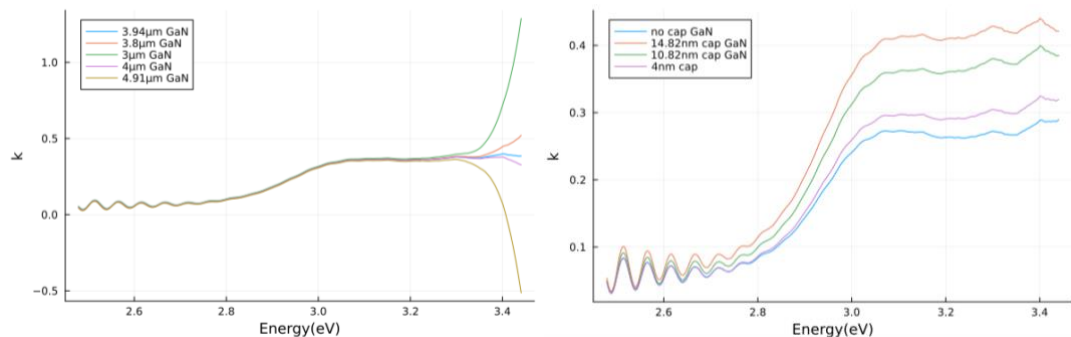4. GaN layer thickness and the InGaN extinction coefficient κ

Figure 14. Computed InGaN extinction coefficient κ as a function of energy (eV) on 11.5% indium content InGaN sample. Left: plots for different test values for the UID

GaN layer thickness. Right: plots for different test values of the for the cap GaN layer thickness.

The TMM is used on the 11.5% indium content InGaN sample to compute the InGaN extinction coefficient κ. The UID GaN layer was intended to be $4\ \mu m$ thick. However, the actual thickness is variable. The computed InGaN extinction coefficient with multiple "guessed" values of UID GaN layer thickness varying from $3\ \mu m$ to $4.95\ \mu m$, whereas the intended layer thickness is around. From the left plot on Fig. 14, the thickness induces only small variations in the amplitudes of the Fabry-Pérot fringes far away from the GaN absorption edge. Generally, the amplitudes of the Fabry-Pérot fringes decrease close to the InGaN absorption edge at around $2.8\ eV$. More importantly, the InGaN κ is very sensitive to the UID GaN layer thickness GaN absorption edge ($\sim 3.4\ eV$).

Relying on the logic that InGaN κ should not be divergent around the GaN absorption edge, the "guessed" thickness that yields stable InGaN κ at that region is retained. Despite this, its accuracy does not seem to affect the amplitudes or the shape of the InGaN energy dependent κ curve. Hence, the bandgap extrapolation from the resulting Tauc plot would not be affected by this parameter. It would not affect the magnitude of the InGaN absorption coefficient either.

The same simulation is done to same sample to see the effect of varying cap GaN layer thickness on the InGaN κ as shown on the right plot of Fig. 14. The Rigaku HRXRD fitted cap GaN layer thickness is $10.82\ nm$ for reference. The tested values for the cap GaN layer thickness range from $0\ nm$ to $14.82\ nm$. The amplitudes of the InGaN κ are rather sensitive to the variation in the cap GaN layer thickness, which would affect the slope at the InGaN

absorption edge hence the value of the InGaN bandgap. The InGaN absorption coefficient would also suffer considerable variations from the cap GaN layer thickness inaccuracy.

B. InGaN absorption coefficient and bowing parameter values

1. Results from TMM

From four InGaN samples of 8.1%, 9.6%, 11.5% and 14.3% indium contents, the absorption coefficients and a bowing parameter value for this composition range were produced. The tabulated sample information, the HRXRD peak fitting for the material composition and the Tauc plots are found in Appendix A, B and D respectively. The InGaN layers on all samples are coherently grown on the GaN based on RSM analysis (angle maps in Appendix C).
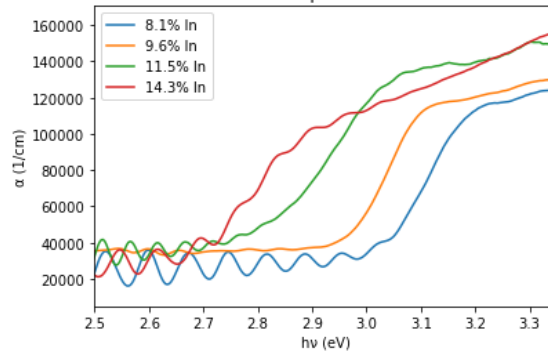
Figure 15. Plot of TMM extracted InGaN absorption coefficient (cm^{-1}) as a function of energy (eV).

The extrapolation of the InGaN extinction coefficients using the TMM (cf. Section II-B-5) follows the same procedure as delineated before for the extrapolation of the GaN absorption coefficients. The following assumptions still apply: the GaN layer is treated as incoherent, and the substrate is treated as a semi-infinite medium. The stack of materials in the order of forward wave propagation is: Al_2O_3, UID GaN, InGaN, cap GaN, air. The measured InGaN

transmittance are equated to the TMM calculated expression, a function of the InGaN extinction coefficient. The nonlinear equation is then solved in with Julia's "nlsolve" function. The extrapolated GaN extinction coefficient is used instead of values from Adachi[41] . The extinction coefficients of GaN and Sapphire are shown in Appendix E. The energy dependent refractive index used is shown in Appendix F.

The InGaN absorption coefficients are obtained using the extracted InGaN extinction coefficients and Eq.12. The oscillations in the curves on Fig 15. are likely due to the thick UID GaN layer. It is possible that it causes a partial coherence as observed previously, since there is a phase shift between the measured reflected and transmitted beams as shown on Fig. 12. The order of magnitude in the InGaN α seems coherent with existing literature[11,42].
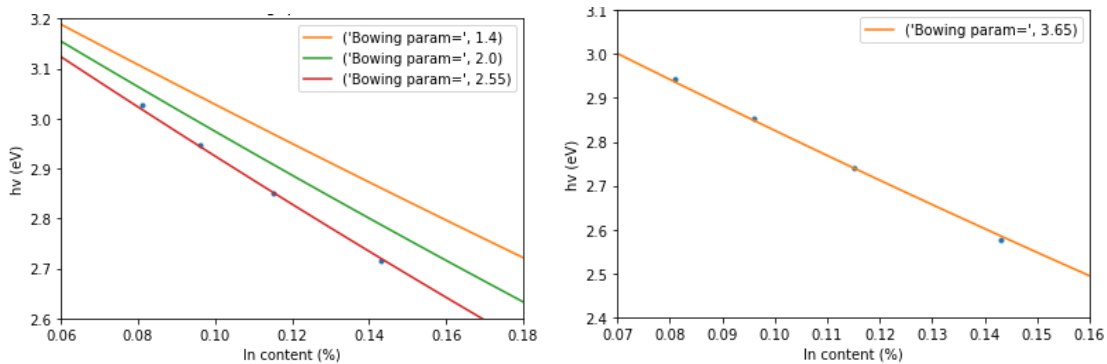

Figure 16. TMM extracted InGaN bandgap energy curves. Left: Plot of the non-strain adjusted InGaN bandgap energy (eV) as a function of indium content (%). Three values of bowing parameter are used the InGaN bandgap energy equation (Eq. 37) to produce the curves. Right: Plot of the strain corrected InGaN bandgap energy with the bowing parameter $3.65eV$.

The Tauc plots for each measured sample are generated from the absorption coefficients. The bandgap energies are extracted from the Tauc plots (cf. Section II-B-6), and strain adjusted

(cf. Section II-B-8). They are plotted as a function of their corresponding percent indium content along with the plot of the InGaN bandgap energy equation (Eq. 37) in the low indium content range between 7% and 16% as shown on the right plot of Fig.16. The non-strain adjusted version of this plot is shown on the left plot of Fig. 16 with curves representing the InGaN bandgap energy equation with three values ($1.4eV$, $2.0eV$ and $2.55eV$) for the bowing parameter plugged into it. The best-fit non-strain adjusted bowing parameter is $2.55\ eV$. One the other hand, the curve that best fits the strain adjusted bandgap energies is the one for a bowing parameter of $3.65\ eV$.

2. Comparison with results from the single slab approximation

The TMM obtained InGaN bowing parameter value can be compared to results using the single slab infinite internal reflection summation method (cf. Section II-B-4) which treats the multilayer InGaN structure as a single slab of material in which the InGaN layer is the only absorptive layer. This approximation is valid for energies below the GaN absorption edge ($< 3.3\ eV$ is a safe assumption). Fig. 17 shows the resulting InGaN bandgap energies of the same four samples plotted as a function of their respective percent indium content.
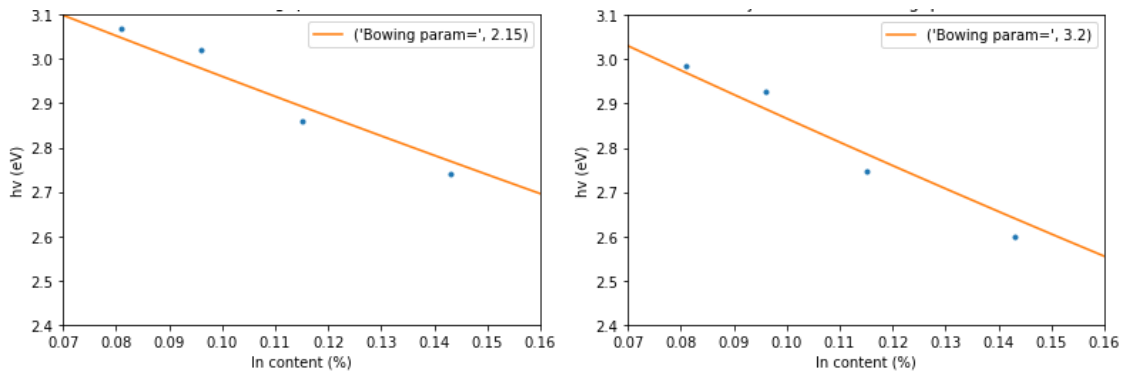

Figure 17. InGaN bowing parameter (eV) fitted bandgap energy (eV) as a function of indium content (%) in the low indium composition range ($7\% \leq x \leq 16\%$) from the

single slab approximation. Left: Plot of the InGaN bandgap energy equation (Eq. 37) using bowing parameter $2.15eV$ with non-strain adjusted bandgap energies. Right: Plot of the same equation using bowing parameter $3.2eV$ with strain adjusted bandgap energies.

The InGaN bowing parameter for the low indium composition range ($7\% \leq x \leq 16\%$) is $2.15eV$ for fully strained InGaN structures as shown on the left plot of Fig.17 and $3.2eV$ for fully relaxed InGaN structures as shown on the right plot of Fig.17.

These values are both lower than the ones from the TMM analysis. The data points also do not align well with the best fit curve. This inconsistency comes from the fact that the GaN contribution to the absorption coefficients were not subtracted in the previous method. Additionally, the InGaN energy dependent refractive index was not accounted for. These prove to have a significant effect. Therefore, the TMM is the superior method for analyzing optical transmittance data to extract the absorption coefficient of just the InGaN layer.

As an aside, the sample indium content was alternatively obtained using K. Jorgensen's code (cf. Section II-B-2). Since the cap GaN layer turned out to have non negligeable effects to shifting the position of the Bragg peaks, the estimated InGaN thicknesses were inaccurate compared to results produced using Rigaku's HRXRD plug-in. Only the results from the latter technique were retained.

C. Shortcomings and suggestions for future work

In the future, the samples could be grown under identical conditions to compensate for the layer thickness variation and any strain discrepancy. The partial coherent interference from

the UID GaN layer could be corrected. Experiments could be repeated for series of different compositional ranges to get composition dependent bowing parameter values.

Further, alternative fabrication methods could be employed to produce stand-alone InGaN membranes. Pulsed-excimer laser lift-off[43] could be an option to consider for instance.

The extraction of the bandgap from the Tauc plot also presents a challenge since identifying the linear part of the plot implies the subjectivity of the human data analyst. Highly reliable automated algorithms could be used instead. One such bandgap extraction method[44] for instance uses the best weighted linear segment after applying a multivariate adaptive regression splines (MARS) regression analysis and a Savitzky-Golay noise filter. Nonetheless, it is known that this method still yields inconsistent results when compared with human expert estimated bandgap values from identical data. Further development on this front could be explored.

IV. Conclusion

The present study successfully measured and analyzed four MOCVD grown InGaN samples with low indium content ($8\% \leq x \leq 15\%$) to obtain the bowing parameter value in this composition range. Using the TMM, the fully strained InGaN samples yielded a bowing parameter value of $2.55\ eV$. The strain corrected bowing parameter values is $3.65\ eV$. These results are consistent with some experimental and theoretical results from current literature[8,9]. The TMM is a better method to extract InGaN absorption coefficient from the multilayer heterostructure optical transmittance measurements compared to the single slab approximation method which gave the bowing parameters of $2.15eV$ and $3.2eV$ for fully strained and strain corrected InGaN structures respectively.

The TMM is the superior method of the two in that it accounts for all constituent layer's energy dependent complex refractive indices and layer thicknesses without neglecting the contributions of the other material layers to the InGaN absorption coefficient.

Several characteristics of the present work help address sources of inaccuracies[9] both experimentally and analytically. The experimental optical transmittance measurement in this work prevents the misevaluation of the bandgap energies due to the Stoke shift present in InGaN LEDs. The use of the RSM and Rigaku HRXRD plug-in provide an adequate estimation of the structure, strain and composition of the localized sample area being tested. The sample area is localized via a custom-made anodized aluminum mask and the X-ray beam size is reduced to size match the exposed area. The data analysis in the present work is based on coherence sensitive TMM and considers the elimination of the GaN contribution to the InGaN absorption coefficients and the energy dependent refractive index of different layers.

The results then produce high quality InGaN Tauc plots for bandgap energy extraction. The derived bowing parameter is then strain corrected.

Further works include perfecting the similarity in the structure of the samples used and explore larger composition ranges. The partial coherence from the UID GaN layer could be corrected. Isolating the pure InGaN layer for experimentation and finding a more reliable Tauc plot bandgap extraction technique or alternative bandgap extraction methods could be considered.

Bibliography

[1] Joe Doyle, *User's Guide for the Shimadzu UV 3600 UV-Vis-NIR Spectrometer* (Santa Barbara, 2012).

[2] J.I. Pankove, *Optical Processes in Semiconductors* (Dover Publications, Inc., New York, 1975).

[3] C.-K. Li, M. Piccardo, L.-S. Lu, S. Mayboroda, L. Martinelli, J. Peretti, J.S. Speck, C. Weisbuch, M. Filoche, and Y.-R. Wu, "Localization landscape theory of disorder in semiconductors. III. Application to carrier transport and recombination in light emitting diodes," Phys Rev B **95**(14), 144206 (2017).

[4] R. Kudrawiec, M. Siekacz, M. Kryśko, G. Cywiński, J. Misiewicz, and C. Skierbiszewski, "Contactless electroreflectance of InGaN layers with indium content ≤36%: The surface band bending, band gap bowing, and Stokes shift issues," J Appl Phys **106**(11), 113517 (2009).

[5] J. Wu, W. Walukiewicz, K.M. Yu, J.W. Ager, E.E. Haller, H. Lu, and W.J. Schaff, "Small band gap bowing in In1−xGaxN alloys," Appl Phys Lett **80**(25), 4741–4743 (2002).

[6] E. Sakalauskas, Ö. Tuna, A. Kraus, H. Bremers, U. Rossow, C. Giesen, M. Heuken, A. Hangleiter, G. Gobsch, and R. Goldhahn, "Dielectric function and bowing parameters of InGaN alloys," Physica Status Solidi (b) **249**(3), 485–488 (2012).

[7] M. Moret, B. Gil, S. Ruffenach, O. Briot, Ch. Giesen, M. Heuken, S. Rushworth, T. Leese, and M. Succi, "Optical, structural investigations and band-gap bowing parameter of GaInN alloys," J Cryst Growth **311**(10), 2795–2797 (2009).

[8] G. Orsal, Y. El Gmili, N. Fressengeas, J. Streque, R. Djerboub, T. Moudakir, S. Sundaram, A. Ougazzaden, and J.P. Salvestrini, "Bandgap energy bowing parameter of strained and relaxed InGaN layers," Opt Mater Express **4**(5), 1030 (2014).

[9] C.G. Van de Walle, M.D. McCluskey, C.P. Master, L.T. Romano, and N.M. Johnson, "Large and composition-dependent band gap bowing in InxGa1−xN alloys," Materials Science and Engineering: B **59**(1–3), 274–278 (1999).

[10] P.G. Moses, and C.G. Van de Walle, "Band bowing and band alignment in InGaN alloys," Appl Phys Lett **96**(2), 021908 (2010).

[11] S.A. Kazazis, E. Papadomanolaki, M. Androulidaki, M. Kayambaki, and E. Iliopoulos, "Optical properties of InGaN thin films in the entire composition range," J Appl Phys **123**(12), 125101 (2018).

[12] S. Chichibu, T. Azuhata, T. Sota, and S. Nakamura, "Luminescences from localized states in InGaN epilayers," Appl Phys Lett **70**(21), 2822–2824 (1997).

[13] K.P. O'Donnell, R.W. Martin, and P.G. Middleton, "Origin of Luminescence from InGaN Diodes," Phys Rev Lett **82**(1), 237–240 (1999).

[14] P.R.C. Kent, and A. Zunger, "Carrier localization and the origin of luminescence in cubic InGaN alloys," Appl Phys Lett **79**(13), 1977–1979 (2001).

[15] L.-W. Wang, "Calculations of carrier localization in InxGa1−xN," Phys Rev B **63**(24), 245107 (2001).

[16] R. People, and J.C. Bean, "Calculation of critical layer thickness versus lattice mismatch for Ge$_x$Si$_{1-x}$/Si strained-layer heterostructures," Appl Phys Lett **47**(3), 322–324 (1985).

[17] L.A. Coldren, S.W. Corzine, and M.L. Mašanović, *Diode Lasers and Photonic Integrated Circuits* (John Wiley & Sons, Inc., Hoboken, NJ, USA, 2012).

[18] Rigaku Corporation, *SmartLab Studio II HRXRD Plugin User Manual* (n.d.).

[19] M. Dudley, and X.R. Huang, in *Encyclopedia of Materials: Science and Technology* (Elsevier, 2001), pp. 9813–9825.

[20] T. Deguchi, D. Ichiryu, K. Toshikawa, K. Sekiguchi, T. Sota, R. Matsuo, T. Azuhata, M. Yamaguchi, T. Yagi, S. Chichibu, and S. Nakamura, "Structural and vibrational properties of GaN," J Appl Phys **86**(4), 1860–1866 (1999).

[21] W. Paszkowicz, "X-ray powder diffraction data for indium nitride," Powder Diffr **14**(4), 258–260 (1999).

[22] A. Krost, G. Bauer, and J. Woitok, in *Optical Characterization of Epitaxial Semiconductor Layers* (Springer Berlin Heidelberg, Berlin, Heidelberg, 1996), pp. 287–391.

[23] T.G. Mayerhöfer, S. Pahlow, and J. Popp, "The Bouguer-Beer-Lambert Law: Shining Light on the Obscure," ChemPhysChem **21**(18), 2029–2046 (2020).

[24] J.C. Richmond, "Relation of emittance to other optical properties," Journal of Research of the National Bureau of Standards, Section C: Engineering and Instrumentation **67C**(3), 217 (1963).

[25] P. Peumans, A. Yakimov, and S.R. Forrest, "Small molecular weight organic thin-film photodetectors and solar cells," J Appl Phys **93**(7), 3693–3723 (2003).

[26] L.A.A. Pettersson,) Lucimara, S. Roman, and O. Inganä, *Modeling Photocurrent Action Spectra of Photovoltaic Devices Based on Organic Thin Films* (1999).

[27] C.C. Katsidis, and D.I. Siapkas, *General Transfer-Matrix Method for Optical Multilayer Systems with Coherent, Partially Coherent, and Incoherent Interference* (2002).

[28] C. Akcay, P. Parrein, and J.P. Rolland, "Estimation of longitudinal resolution in optical coherence imaging," Appl Opt **41**(25), 5256 (2002).

[29] M.S. Dresselhaus, *Solid State Physics Part II Optical Properties of Solids* (1999).

[30] E. Hecht, *Optics* (Addison-Wesley, 2002).

[31] J. Tauc, "Optical properties and electronic structure of amorphous Ge and Si," Mater Res Bull **3**(1), 37–46 (1968).

[32] L. Vegard, "Die Konstitution der Mischkristalle und die Raumfüllung der Atome," Zeitschrift Für Physik **5**(1), 17–26 (1921).

[33] J. Wu, W. Walukiewicz, W. Shan, K.M. Yu, J.W. Ager, S.X. Li, E.E. Haller, H. Lu, and W.J. Schaff, "Temperature dependence of the fundamental band gap of InN," J Appl Phys **94**(7), 4457–4460 (2003).

[34] Y. Nanishi, Y. Saito, and T. Yamaguchi, "RF-Molecular Beam Epitaxy Growth and Properties of InN and Related Alloys," Jpn J Appl Phys **42**(Part 1, No. 5A), 2549–2559 (2003).

[35] S.P. Fu, T.T. Chen, and Y.F. Chen, "Photoluminescent properties of InN epifilms," Semicond Sci Technol **21**(3), 244–249 (2006).

[36] J.I. Pankove, "GaN: from fundamentals to applications," Materials Science and Engineering: B **61–62**, 305–309 (1999).

[37] W. Shan, R.J. Hauenstein, A.J. Fischer, J.J. Song, W.G. Perry, M.D. Bremser, R.F. Davis, and B. Goldenberg, "Strain effects on excitonic transitions in GaN: Deformation potentials," Phys Rev B **54**(19), 13460–13463 (1996).

[38] S. Adachi, *Optical Constants of Crystalline and Amorphous Semiconductors* (Springer US, Boston, MA, 1999).

[39] Sopra S.A., "Sopra Material Database," (n.d.).

[40] "UCSB SSLEEC Material database," (n.d.).

[41] S. Adachi, *Optical Constants of Crystalline and Amorphous Semiconductors* (Springer US, Boston, MA, 1999).

[42] S. Nacer, and A. Aissat, "Simulation and optimization of current matching double-junction InGaN/Si solar cells," Applied Physics A **122**(2), 138 (2016).

[43] W.S. Wong, T. Sands, N.W. Cheung, M. Kneissl, D.P. Bour, P. Mei, L.T. Romano, and N.M. Johnson, "Fabrication of thin-film InGaN light-emitting diode membranes by laser lift-off," Appl Phys Lett **75**(10), 1360–1362 (1999).

[44] M. Schwarting, S. Siol, K. Talley, A. Zakutayev, and C. Phillips, "Automated algorithms for band gap analysis from optical absorption spectra," Materials Discovery **10**, 43–52 (2017).

Appendix

A. Sample information

Sample ID	Rigaku fitted Cap GaN (nm)	InGaN thicknesses (nm)	Indium % Rigaku fitting
200812DS	12.75	46.22	8.1
181213EH	9	58.91	9.6
210621DH	10.82	24.95	11.5
200814BS	10.22	49	14.3

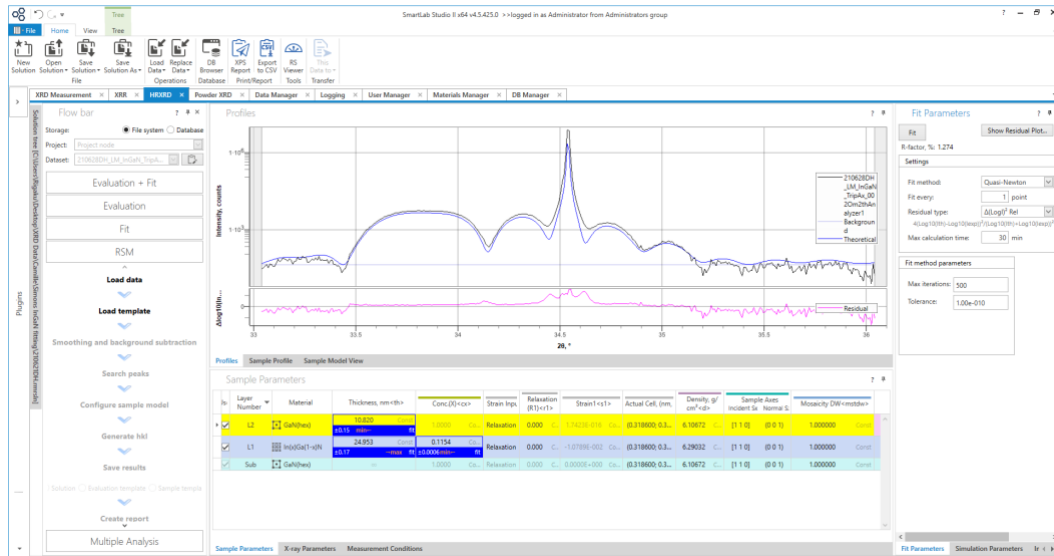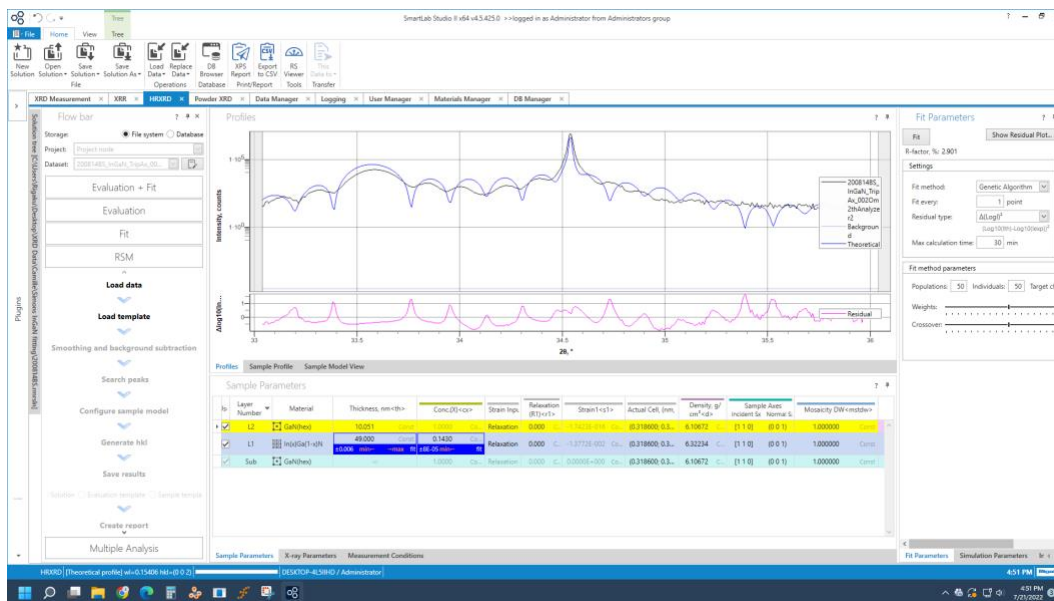B. HRXRD indium content and layer thickness rocking curve fitting
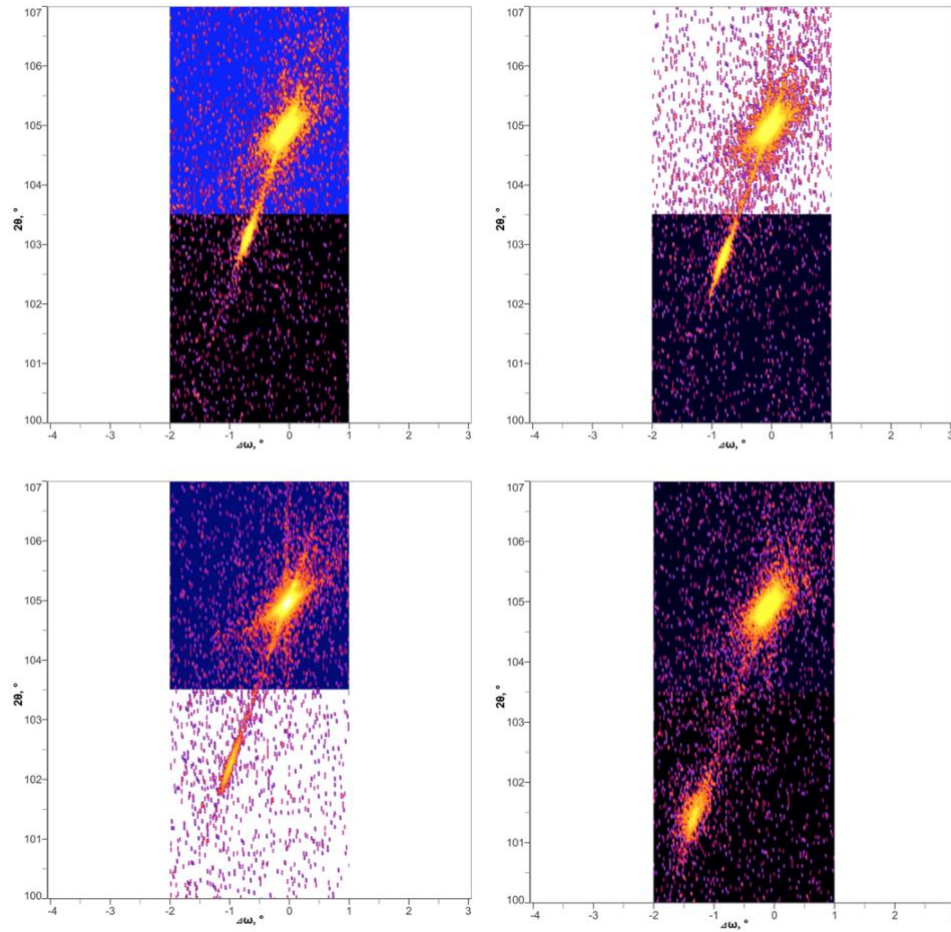
8.1% In InGaN sample:
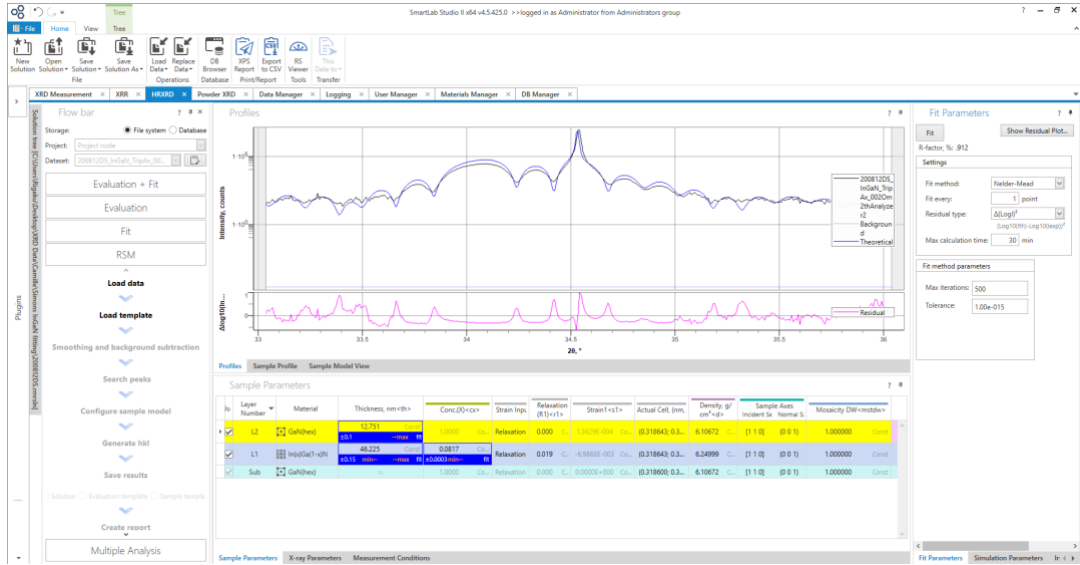
9.6% In InGaN sample:
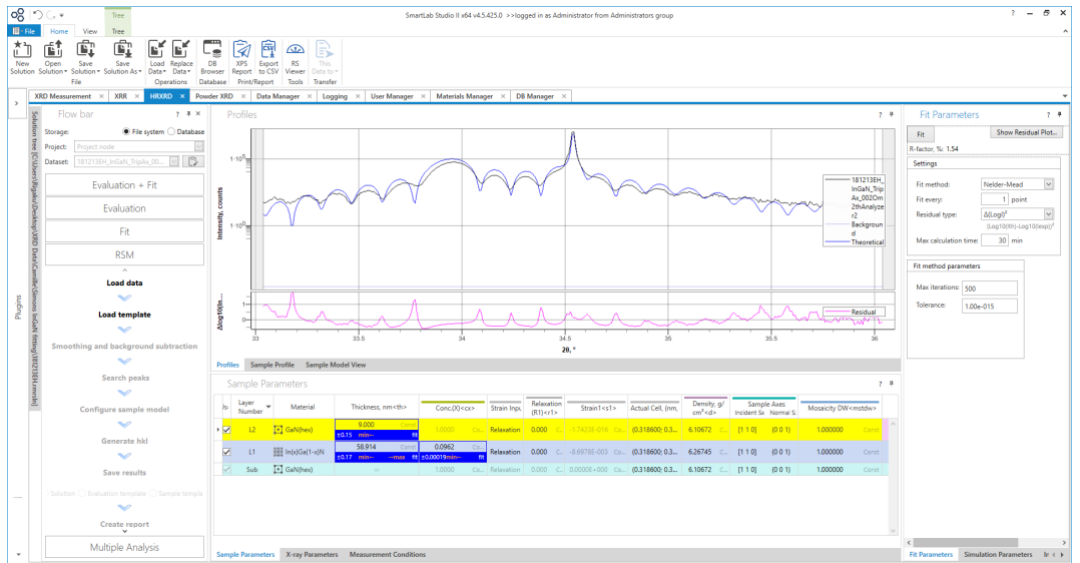
11.5% In InGaN sample:

14.3% In InGaN sample:
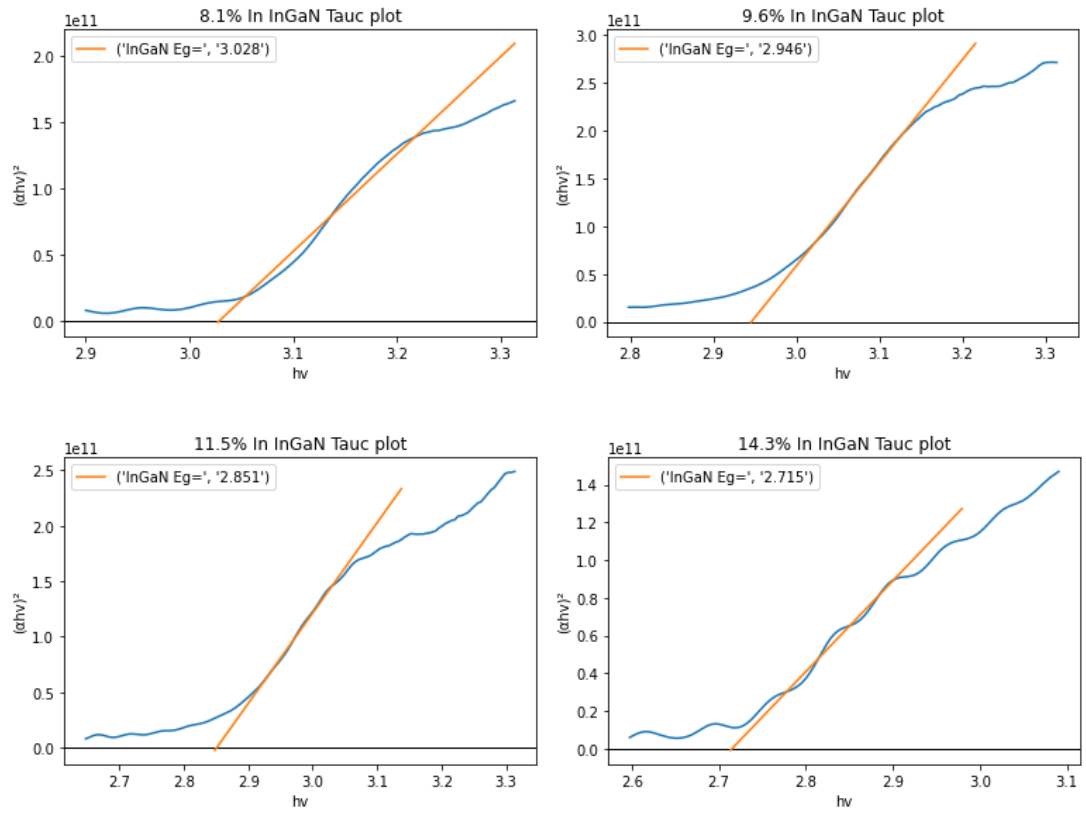
C. Angle maps

Top left: Angle map of the 8.1% In InGaN sample

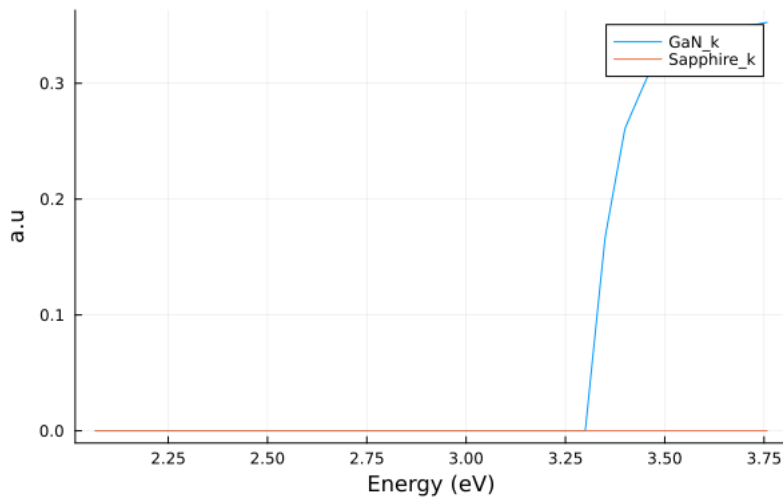Top right: Angle map of the 9.6% In InGaN sample

Bottom left: Angle map of the 11.5% In InGaN sample

Bottom right: Angle map of the 14.3% In InGaN sample

D. Tauc plot

E. Sapphire and GaN extinction coefficient from literature

F. InGaN energy dependent refractive index